Geophysical Journal International

Geophys. J. Int. (2011) **184,** 1–11 doi: 10.1111/j.1365-246X.2010.04821.x

A continuum mechanics approach to quantify brittle strain on weak faults: application to the extensional reactivation of shallow dipping discontinuities

Emmanuel Lecomte,[1,2] Laetitia Le Pourhiet,[1,2] Olivier Lacombe[1,2] and Laurent Jolivet[1,2,3]

[1] *UPMC Univ Paris* 06, *UMR* 7193, *ISTEP,* F-75005, *Paris, France. E-mail: emmanuel.lecomte@upmc.fr*
[2] *CNRS, UMR* 7193, *ISTEP,* F-75005, *Paris, France*
[3] *ISTO, Université d'Orléans-CNRS, UMR* 6113, F-45071 *Orléans, France*

Accepted 2010 September 22. Received 2010 August 27; in original form 2009 November 11

SUMMARY

A number of field observations suggest that sliding on fault planes may occur at very shallow dip in the brittle field. The existence of active low angle normal faults is much debated because (1) the classical theory of fault mechanics implies that faults are locked when the dip is less than 30° and (2) shallow dipping fault planes do not produce large earthquakes ($M > 5.5$). To reconcile observations and theory, we propose a new model for fault reactivation by introducing an elasto-plastic frictional fault gouge as an alternative to the classical dislocation models with frictional properties. Contrary to the classical model which implies that the dilation angle ψ equals the friction angle ϕ, our model accounts for $\psi < \phi$ and permits $\psi < 0$ in the fault gouge as deduced from laboratory and field observations. Whilst the predicted locking angles differ in most cases by less than 10° from the classical model, a significant amount of plastic strain (strain occurring in elasto-plastic regime) is predicted to occur on badly oriented faults prior to locking in a strain-hardening regime. We describe four modes of reactivation which include complete/partial reactivation with/without tensile failure in the surrounding medium. This paper presents analytical solutions to separate those four different modes as well as numerically computed estimates of the amount of plastic strain accumulated before locking. We conclude that plastic strain on badly oriented faults is favoured by compaction of the fault gouge and that those faults are probably aseismic because this strain always occurs in a hardening regime.

Key words: Creep and deformation; Fault zone rheology; Rheology and friction of fault zones; Fractures and faults.

1 INTRODUCTION

Some low angle normal faults (LANFs) preserve field evidence for brittle-frictional behaviour, for example, a brecciated gouge. These faults are often associated with vertical joints and veins, which show that deformation occurred while the maximum principal stress was nearly vertical (e.g. Collettini & Barchi 2002; Skarpelis 2002; Famin *et al.* 2004; Mehl *et al.* 2005). Therefore, those faults can be classified as 'weak' faults in the sense that they occur at large angle (>45°) with respect to the maximum compressive stress σ_1. Studying weak LANFs presents several advantages compared to their strike-slip equivalents (e.g. San Andreas fault). First, exhumation processes and/or uplift produce vertical displacement, which allow fault zone, processes that occurred at different depths to be observed at the outcrop scale. Secondly, boundary conditions (i.e. the direction of the principal stresses) are not well constrained on strike-slip faults while, during the activity of the LANF, one component of stress acting on the fault plane is known because the vertical stress (ρgz) is not contained within the fault plane.

Exhumed LANFs are widespread and frequently associated with metamorphic core complexes (Wernicke 1992). Some of them are seismically active (Abers *et al.* 1997). However, it is rare to observe earthquakes with significant magnitude ($>M$ 5.5) on those faults (McKenzie 1969; Jackson & White 1989; Collettini & Sibson 2001).

It is beyond the scope of this study to discuss whether such structures were formed at low angle in the ductile field (Lister & Davis 1989), or correspond to reactivated ancient thrusts or rotated high angle normal faults (Wernicke 1981; Buck 1988). Similarly, processes which allow a decrease of the friction coefficient of the fault, such as the presence of talc in the fault gouge (Moore & Rymer 2007) or fluid overpressure (Rice 1992), are not considered here. Instead we focus on the parameters, which favour elasto-plastic deformation to occur on an extensionally reactivated pre-existing low angle-dipping plane. The originality of our approach is that

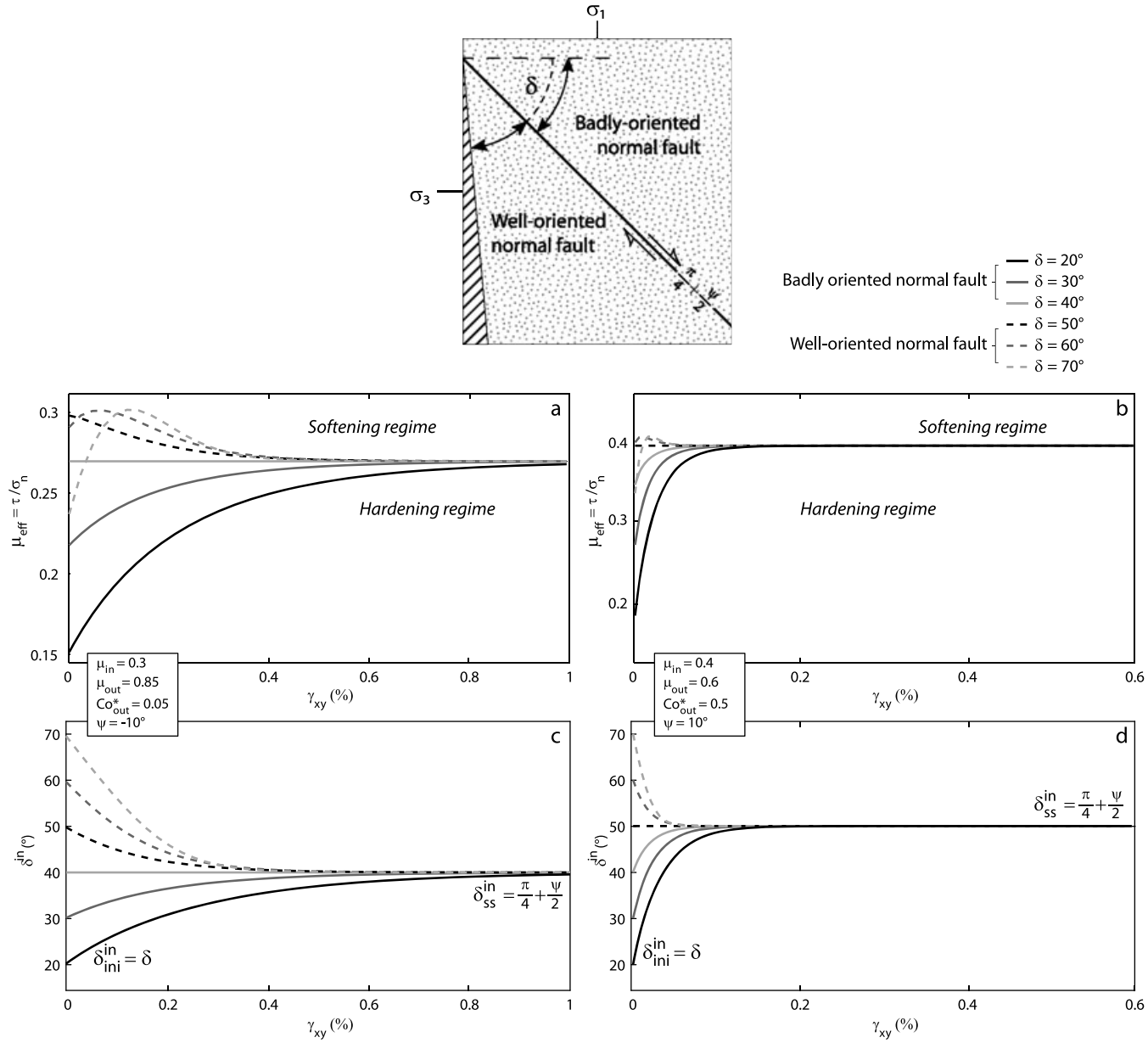

Figure 1. Effective friction evolution (a and b) and stress rotation within the shear zone (c and d) during shearing along a normal fault with varying dip. The strength of the fault depends on whether the dip of the fault is higher or lower than a critical dip of $\pi/4 + \psi/2$. The fault may evolve in a strain softening (well-oriented fault) regime or in a strain hardening (badly oriented fault) regime. In the first case, the effective friction of the fault decreases from a peak value to a steady state one whereas in the second case, the effective friction of fault increases up to a steady state value.

the faults are modelled as thin layers or shear zones, which deform with an elasto-plastic rheology (Vermeer 1990), rather than as dislocations with frictional properties. This approach allows the evolution of stresses to be modelled within the shear zone and in the embedding medium when plastic flow occurs. The main difference with the classical reactivation model lies in the possibility to quantify the amount of plastic strain within the shear zone before it locks. This elasto-plastic formulation has already been used for many geological problems (Poliakov *et al.* 1993; Gerbault *et al.* 1999; Chéry 2001) and can be applied to all fault orientations (Fig. 1 and Supporting Information). Vermeer (1990) showed that the stress evolution during the slip on a reverse fault ($\sigma_3 =$ *constant* = vertical) depends mainly on the dip of the fault. Here, we adopt a similar formulation for normal faults ($\sigma_1 =$ *constant* = vertical). We find that depending whether the dip of fault is higher or lower than a critical dip of $\frac{\pi}{4} + \frac{\psi}{2}$ (ψ characterizing the dilation angle of the fault), the fault may evolve in a strain softening (well oriented fault) or strain-hardening (badly oriented fault) regime (Fig. 1). The strength of a well oriented fault decreases from an initial peak value to a steady state one whereas the strength of badly oriented faults increases with strain up to a steady state value. In both cases the strength changes due to the rotation of the principal stress axes within the shear zone. The rotation continues until the maximal principal stress axis σ_1 reaches the limiting angle of $\frac{\pi}{4} + \frac{\psi}{2}$ with the shear zone (Fig. 1), defining the steady state of the system. Our formulation is compatible with the model proposed by Byerlee & Savage (1992), which suggested a limiting angle of $\frac{\pi}{4}$, according to a dilation angle equal to zero.

We present first the mathematical model used for computing the stress evolution with increasing shear strain within and outside the shear zone and second the results of a parametric numerical analysis. The predictions of the model in terms of plastic strain and stress rotation are discussed in the light of tectonic markers potentially observed within natural LANF zones (e.g. secondary shears) or in the surrounding medium (e.g. vertical veins and/or meso-scale high angle normal faults). The paper further provides analytical solutions that define the transition between the different structural patterns associated with slip on the shallow-dipping plane as a function of the rheological parameters.

2 PARAMETRIC AND NUMERICAL ANALYSIS

2.1 Conceptual model

The shear zone is considered as a pre-existing thin layer of dip δembedded in a brittle medium (Fig. 2a). Both media are characterised by five mechanical parameters. The Poisson ratio υ and the shear modulus Gcharacterise their elastic properties. The friction angle ϕ, the dilation angle ψ and the cohesion Co characterize their plastic properties. The superscripts in and out refer to parameters

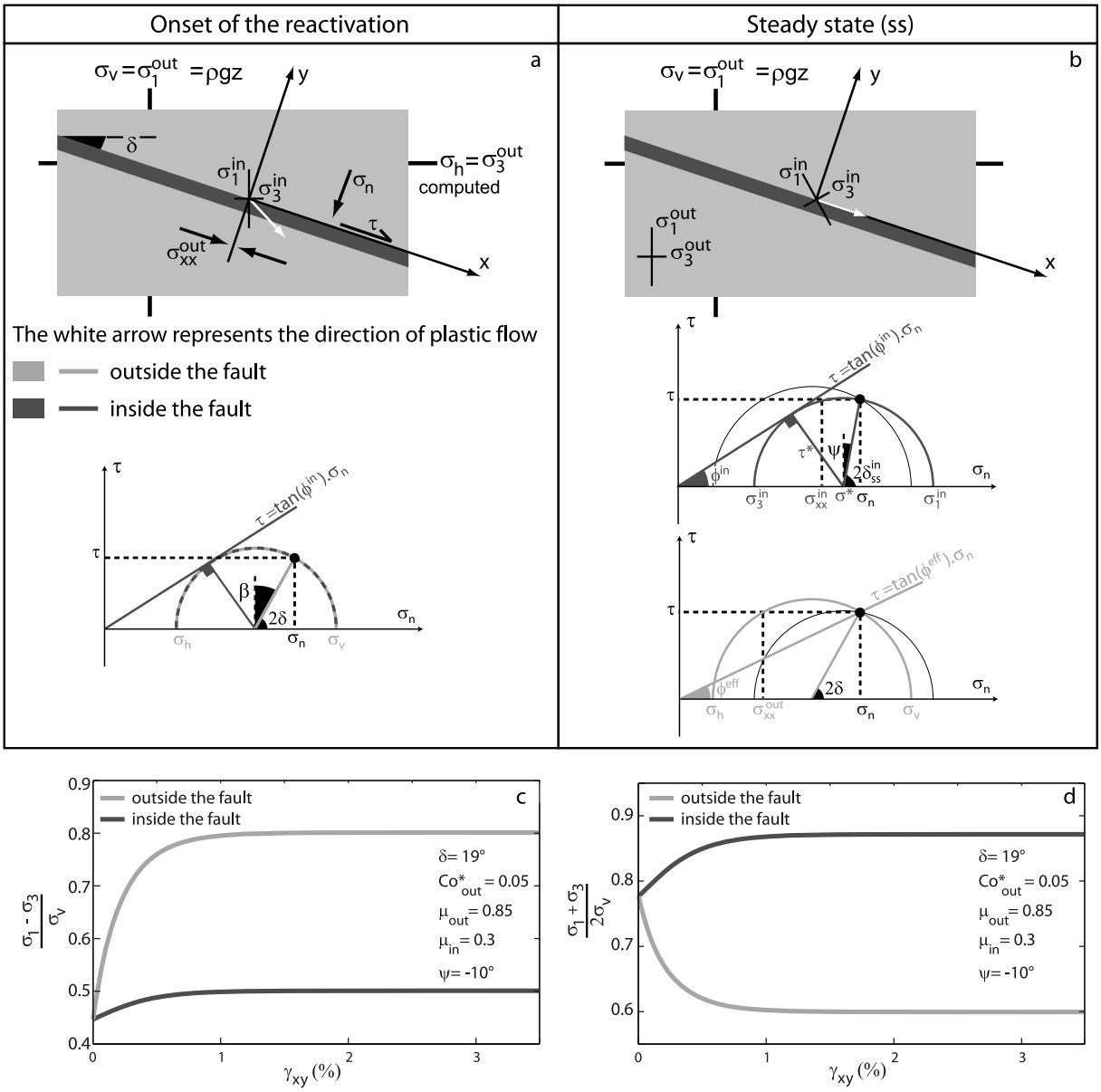

Figure 2. (a) and (b) Setup of the model and Mohr circle constructions representing the state of stress within and outside the shear zone. At the onset of the localisation, stresses within and outside the shear zone are equal (a). During localisation, the stress within the shear zone rotates from an orientation depending initially on the dip of the shear zone δ, to an orientation depending on the dilation angle, $\delta_{ss}^{in} = \frac{\pi}{4} + \frac{\psi}{2}$ (Fig. 1). (c) and (d) Evolution of the differential stress and the pressure within and outside the shear zone, respectively. Differential stress and pressure are normalized to the lithostatic pressure. (e) Evolution of the effective friction of the fault including a variation of the elastic properties between the fault zone and the embedded medium during elasto-plastic deformation.

within and outside the shear zone, respectively. The stress and strain rate tensors are written using the Voigt notation.

The surroundings of shallow dipping normal faults are commonly subject to coeval occurrence of vertical veins and cracks (e.g. Mehl *et al.* 2005). These observations attest for a sub-vertical maximum principal stress $\sigma 1$ during the activity of the fault, which allows to use the Anderson's principle (Anderson 1951). Therefore, we consider that the maximum principal stress outside the shear zone is vertical and equal to the lithostatic pressure, as described by eq. 1:

$$\sigma_1^{out} = \sigma_v = \int_0^z \rho(z) g dz, \tag{1}$$

where g is the Earth's gravitational acceleration and $\rho(z)$ the density at depth z. The shear zone defines a local orthonormal $x - y$ reference frame, in which the x-axis is parallel to the shear zone. The dip of the shear zone, δ, is equal to the angle between the shear zone and the minimum principal stress σ_3^{out}.

The stress and strain rates are homogenous inside and outside the shear zone. Between the shear zone and the embedding medium, the shear and normal components of stress acting on the interface must be continuous, hence:

$$\sigma_n = \sigma_{yy}^{in} = \sigma_{yy}^{out}, \tag{2}$$

$$\tau = \sigma_{xy}^{in} = \sigma_{xy}^{out} \tag{3}$$

and their ratio corresponds to the effective friction as defined by Amonton's law:

$$\mu_{eff} = \tan\phi = \frac{\tau}{\sigma_n}. \tag{4}$$

However, a stress discontinuity is introduced across the interface by allowing σ_{xx} to be discontinuous across the shear zone boundary.

No voids are permitted at the interface between the shear zone and the embedding medium as required in continuum mechanics. Displacements must therefore be compatible, resulting in:

$$\dot{\varepsilon}_{xx}^{in} = \dot{\varepsilon}_{xx}^{out} \tag{5}$$

the two other components of the strain rate, $\dot{\varepsilon}_{yy}$ and $\dot{\varepsilon}_{xy}$, may however be discontinuous across the interface.

The discontinuities included in the model result in different relative angles between the shear zone and the maximum principal stress axis depending on whether the state of stress is considered within or outside the shear zone. The state of stress in the system can be represented with two Mohr circles (Fig. 2) that must cross on the fault plane (σ_n, τ) to fulfil the requirement for continuity (eqs 2 and 3).

2.2 Description of the model

As the $x - y$ reference frame forms an angle δ with the principal stress reference frame, the stress can be written in the $x-y$ reference frame as a function of principal stress and δ:

$$\boldsymbol{\sigma}^{out} = \begin{bmatrix} \sigma_{xx}^{out} \\ \sigma_{yy}^{out} \\ \sigma_{xy}^{out} \end{bmatrix} = \frac{1}{2} \begin{bmatrix} \sigma_1^{out}(1 - \cos 2\delta) + \sigma_3^{out}(1 + \cos 2\delta) \\ \sigma_1^{out}(1 + \cos 2\delta) + \sigma_3^{out}(1 - \cos 2\delta) \\ (\sigma_1^{out} - \sigma_3^{out}) \sin 2\delta \end{bmatrix}. \tag{6}$$

In this frame, σ_{yy}^{out} is σ_n and σ_{xy}^{out} is τ. Introducing them into the effective friction definition (eq. 4), we find a linear relationship between σ_1^{out} and σ_3^{out} as a function of the effective friction and the dip of the shear zone:

$$\sigma_3^{out} = \sigma_1^{out} \frac{\sin 2\delta - \mu_{eff}(1 + \cos 2\delta)}{\sin 2\delta + \mu_{eff}(1 - \cos 2\delta)}. \tag{7}$$

As σ_1^{out} is constant and equal to σ_v (Anderson principle), we now aim to compute the effective friction of the shear zone to fully constrain the surrounding state of stress.

To that end, we introduce a yield function and elasto-plastic rheological equations in the model (Vermeer & de Borst 1984; Vermeer 1990).

The model considers that the shear zone is yielding when function $\mathcal{F}^{in}$ equals zero:

$$\mathcal{F}^{in} = \tau^* - \sigma^* \sin\phi^{in} - Co \cos\phi^{in} = 0. \tag{8}$$

Here, τ^* and σ^* correspond to the radius and to the centre of the Mohr circle, respectively:

$$\begin{cases} \tau^* = \dfrac{1}{2}\sqrt{\left(\sigma_{yy}^{in} - \sigma_{xx}^{in}\right)^2 + 4\sigma_{xy}^{in^2}} \\ \sigma^* = \dfrac{1}{2}\left(\sigma_{yy}^{in} + \sigma_{xx}^{in}\right) \end{cases}. \tag{9}$$

The Mohr circle constructions allow the stress state at the onset of yielding to be constrained (Fig. 2a). It is possible to numerically compute the complete stress–strain state within and outside the shear zone as a function of the amount of shear strain γ at a single point in space, following Euler's forward marching integration scheme (Vermeer 1990). The computation accounts for an elasto-plastic behaviour within the shear zone and Hooke's law outside (both rigidity matrices are described in Appendix A). It uses the Anderson principle to fix the boundary conditions with the elastic surrounding medium (eq. 1) while continuity (eqs 2 and 3) and compatibility (eq. 5) conditions allow computation of the evolution of strain and stress within the shear zone.

Since the shear zone is not parallel to the plastic flow direction, part of the deformation within the shear zone is elastic. The elastic strain causes a rotation of the principal stresses (Fig. 2b) in such a way that the angle, β, between the plastic flow and the shear zone decreases with increasing strain ($\beta - \psi \rightarrow 0$). The stress within the shear zone rotates from an orientation depending initially on the dip of the shear zone δ, to an orientation depending on the dilation angle, $\delta_{ss}^{in} = \frac{\pi}{4} + \frac{\psi}{2}$ (Fig. 1).

For the range of tested shear zone orientations ($0^\circ < \delta < 45^\circ$), plastic strain occurs in a hardening regime since the deviatoric stresses within and outside the shear zone increase continually during deformation (Fig. 2c). Notably, the pressure rises within the shear zone, but decreases outside (Fig. 2d). This is consistent with previous models, which describe an increase of mean stress within a badly oriented fault (e.g. Chéry *et al.* 2004).

At large strain, $\beta = \psi$ and the plastic flow is parallel to the shear zone (Fig. 2b), hardening stops and the shear zone now behaves effectively as a perfect plastic body. In the rest of the paper, we will call that final stage the steady state because from that amount of strain onward, the stress does not change anymore.

2.3 Reactivation associated to shear failure in the surrounding medium

In shear we use the Mohr–Coulomb yield criterion to determine whether a new fault can form in the surrounding medium (i.e. for stresses outside the shear zone reaching the yield criterion) before the steady state is established. Based on this approach, Sibson (1990)

described the conditions of reactivation of a fault according to its intrinsic parameters and defined the limit of reactivation as the locking angle of the fault. However, our model allows to constrain the amount of strain which can occur on the shear zone before it locks. We show that plastic strain may take place before the shear zone locks (see Section 2.5), so we prefer to describe the locking angle defined by Sibson (1990) as the limit between partial and total reactivation of the shear zone. We now seek to analytically describe the state of stress at steady state to establish the locking angle for our model. The normal and shear components of stress acting on the shear zone can be written as a function of the stress invariants of the shear zone and the dilation angle:

$$\begin{cases} \tau = \tau^* \cos\psi \\ \sigma_n = \sigma^* - \tau^* \sin\psi \end{cases}. \tag{10}$$

When the shear is yielding, τ^* and σ^* are linearly related (Fig. 2b), so that the effective friction μ_{eff} only depends on the intrinsic parameters of the shear zone ϕ^{in} and ψ, hence:

$$\tau^* = \sigma^* \sin\phi^{in}, \tag{11a}$$

$$\mu_{eff} = \frac{\sin\phi^{in}\cos\psi}{1-\sin\phi^{in}\sin\psi}. \tag{11b}$$

Since σ_v is constant and equal to $\rho g z$ which corresponds to σ_1^{out} in extensional setting, it is possible to actually compute the full steady state stress tensor in the embedding medium as a function of depth. Integrating eq. 11b into eq. 7, the relation between the minimal and the maximal principal stress outside the shear zone becomes:

$$\sigma_3^{out} = \rho g z \frac{\sin 2\delta\,(\sin\phi^{in}\sin\psi - 1) + \sin\phi^{in}\cos\psi(1+\cos 2\delta)}{\sin 2\delta\,(\sin\phi^{in}\sin\psi - 1) - \sin\phi^{in}\cos\psi(1-\cos 2\delta)}. \tag{12}$$

The limit between complete and partial shear zone reactivation is obtained when the system is in a steady state and the outside stress reaches the yield criterion. Using Mohr circles, one can obtain an expression for the minimal principal stress outside the shear zone as a function of the parameters Co^{out} and ϕ^{out} of the surrounding medium given by:

$$\sigma_3^{out} = \sigma_1^{out}\frac{1-\sin\phi^{out} - 2Co^{out}\cos\phi^{out}}{1+\sin\phi^{out}}. \tag{13}$$

Combining eqs 12 and 13, the friction angle of the shear zone can be written as:

$$\sin\phi^{in} = \frac{\mathrm{A}\,\sin 2\delta}{\mathrm{A}\,\cos(\psi - 2\delta) + \cos\psi\left(\sigma_1^{out} - Co^{out}\cos\phi^{out}\right)}, \tag{14}$$

with $A = \sigma_1^{out}\sin\phi^{out} + Co^{out}\cos\phi^{out}$.

Eq. 14 determines the maximal friction angle within the shear zone that allows a complete reactivation of the system (Fig. 3a). We established it as a function of the dip of the shear zone to quantitatively compare our model to the classical brittle models (Sibson 1990; Collettini & Sibson 2001; Fig. 3a black curve). Grey curves on Fig. 3(a) show the locking angle of the fault (i.e. the limit between partial and total reactivation of the fault) according to the dilation angle. One can see that the total reactivation of a compacting shear zone can occur at higher friction coefficients than those defined by Sibson (1990). Nevertheless, severely badly oriented shear zones cannot be reactivated with a friction coefficient higher than 0.1 and other processes, such as fluid overpressure (Rice 1992), are required to reduce the friction coefficient of the fault.

When the dilation angle is equal to the friction angle of the shear zone, that is, in the case of associated plastic flow, the effective friction on the shear zone (eq. 11b) can be written in terms of the embedding media parameters only. Considering the least principal stress σ_3^{out} as given in eq. 12 and combining it with eq. 13, the friction angle within the shear zone required for a complete reactivation is found in eq. 15. It corresponds to Sibson's (1990) definition:

$$\tan\phi^{in} = \frac{\mathrm{A}\,\sin 2\delta}{\mathrm{A}\,\cos 2\delta + \sigma_1^{out} - Co^{out}\cos\phi^{out}}. \tag{15}$$

The effective friction of the shear zone allows us to define the potential reactivation of the shear zone as a function of the reactivation angle $\theta_r = 90^\circ - \delta$ (Sibson 1990); θ_r then corresponds to the angle between the direction of the maximal principal stress outside the shear zone (here, vertical) and the shear zone. Expressing eq. 12 in terms of differential stress and plotting it versus θ_r (Fig. 3b, grey line) allows a direct comparison with the locking angle computed in previous studies (e.g. Collettini & Sibson 2001). The maximum locking angle is obtained for a dilation angle equal to the friction of the shear zone ($\psi = \phi^{in}$) corresponding to an associated plastic flow rule (black line on Fig. 3b). In that case, the shear zone is found to behave exactly like the brittle model (Sibson 1990). Rocks however, typically have $\psi \simeq 0$ and mature faults actually display severe compaction due to grain size reduction (Niemeijer *et al.* 2009). A small to negative dilation angle allows the shear zone to be fully reactivated at smaller dips δ. The grey line on Fig. 3(b) indicates that the maximum dip for the reactivation of a shear zone with a friction angle $\mu^{in} = 0.6$, is close to $\delta \approx 20^\circ$ ($\theta_r \approx 70^\circ$). Hence, taking into account more realistic parameters, we show that the locking angle may differ by up to 10°. This result is obtained assuming an extreme compaction coefficient ($\psi = -\phi^{in}$). However, we note that for small friction values, the coefficient of compaction also remains small.

2.4 Reactivation associated to tensile failure in the surrounding medium

As mentioned earlier, LANF's are frequently associated with tensile failure of the embedding medium. We therefore seek to determine the set of parameters for which shear zone reactivation leads to such tensile failure. The limit between reactivation with or without tension can be characterised by introducing a yield criterion in tension that we simply define as $\sigma_3^{out} \leq 0$. Inserting this failure criterion into eq. 13 and solving for the cohesion of the surroundings, we find that tensile failure only occurs if the following condition is satisfied:

$$Co^{out} \leq \sigma_1^{out}\frac{1-\sin\phi^{out}}{2\cos\phi^{out}}. \tag{16}$$

The limit of the partial reactivation in the context of an embedding medium in tension therefore does not depend on the mechanical properties of the shear zone. However, the limit between complete reactivation in a tensional setting is related to the dip and the intrinsic parameters of the shear zone (eq. 17). To compute it, we substitute eq. 11b into eq. 7 and solve for $\sigma_3^{out} = 0$. The limiting shear zone friction for a complete reactivation of the shear zone associated with tensile failure thus becomes:

$$\sin\phi^{in} = \frac{\sin 2\delta}{\cos\psi(1+\cos 2\delta) + \sin\psi\,\sin 2\delta}. \tag{17}$$

The outcomes of the parametric analysis can therefore be classified into four modes of reactivation to be compared to geological observations.

The modes include a complete (Fig. 4, cases I and II) or partial (Fig. 4, cases III and IV) reactivation of the shear zone with (Fig. 4, cases II and III) or without (Fig. 4, cases I and IV) tensile failure

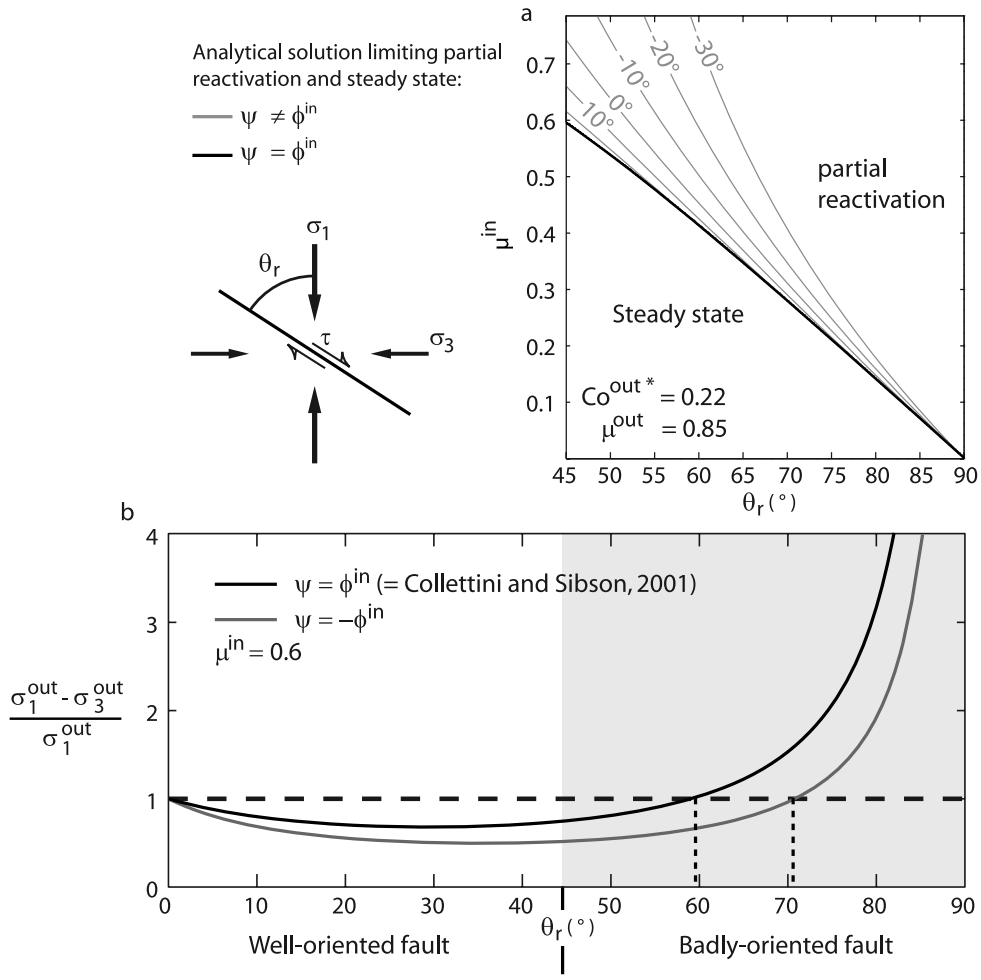

Figure 3. (a) Analytical solution limiting partial reactivation and steady state as a function of the friction and the dip of the shear zone. (b) Analytical solution limiting partial reactivation and steady state as a function the differential stress outside the shear zone and its dip (after Collettini & Sibson 2001).

in the surrounding medium. The partial mode of reactivation define sets of parameters which do not allow a complete reactivation (i.e. the steady state) of the system. In that case, stresses in the embedded media reach the yield criteria; the system is then considered locked.

2.5 Numerical analysis

The numerical model allows the quantification of the plastic strain in partial reactivation mode before the system locks. For each set of parameters, a unique mode of reactivation is found and the numerical analysis is well described by the analytical formula previously derived (Fig. 5). A large range of the set of parameters tested herein do not reach a steady state. Nevertheless, significant plastic strain can occur on the LANF prior to the formation of a new fault. The amount of plastic strain is higher (1) when the system is close to the steady state and (2) for high confining pressure. This amount thus depends on the initial dip of the shear zone and on the intrinsic parameters of the embedding medium.

The limit between the steady state and the partial reactivation (Fig. 5, blue line), defined by eq. 14, depends mainly on the dip of the shear zone and on the ratio between the cohesion outside the shear zone and the confining pressure $Co^{out*} = \frac{Co^{out}}{\sigma_v}$. Increasing Co^{out*} favours the complete reactivation for higher shear zone friction. Therefore, the reactivation at steady state of the system requires a lower shear zone friction for high confining pressure. However, the strain accumulated on the shear zone prior to locking is much higher at high confining pressure and therefore should favour the coexistence of high angle normal faults and LANFs.

Tensile cracks and veins in the embedding medium may develop when the LANF is reactivated, either partially or completely (Fig. 5, pink and green lines). In the case of complete reactivation (no high angle normal fault around), their occurrence is independent of the confining pressure. Interestingly, the coeval occurrence of tensile cracks and high angle normal faults and LANFs (Fig. 5, mode of reactivation III) is only possible for a very small range of parameters.

3 DISCUSSION AND CONCLUSION

3.1 Main results

This contribution formulates a new model for extensional fault reactivation in which faults follow a non-associated Mohr–Coulomb plastic flow, controlled by two parameters: the friction angle ϕ and the dilation angle ψ. This rheological model is used in most of the geodynamic codes to simulate the formation and reactivation of faults in the crust (e.g. Chéry 2001; Le Pourhiet *et al.* 2004) using a dilation angle of zero. In this paper, we derived an analytical solution for fault reactivation using the non-associated plastic flow rule theory. Results include the solution of the classical fault

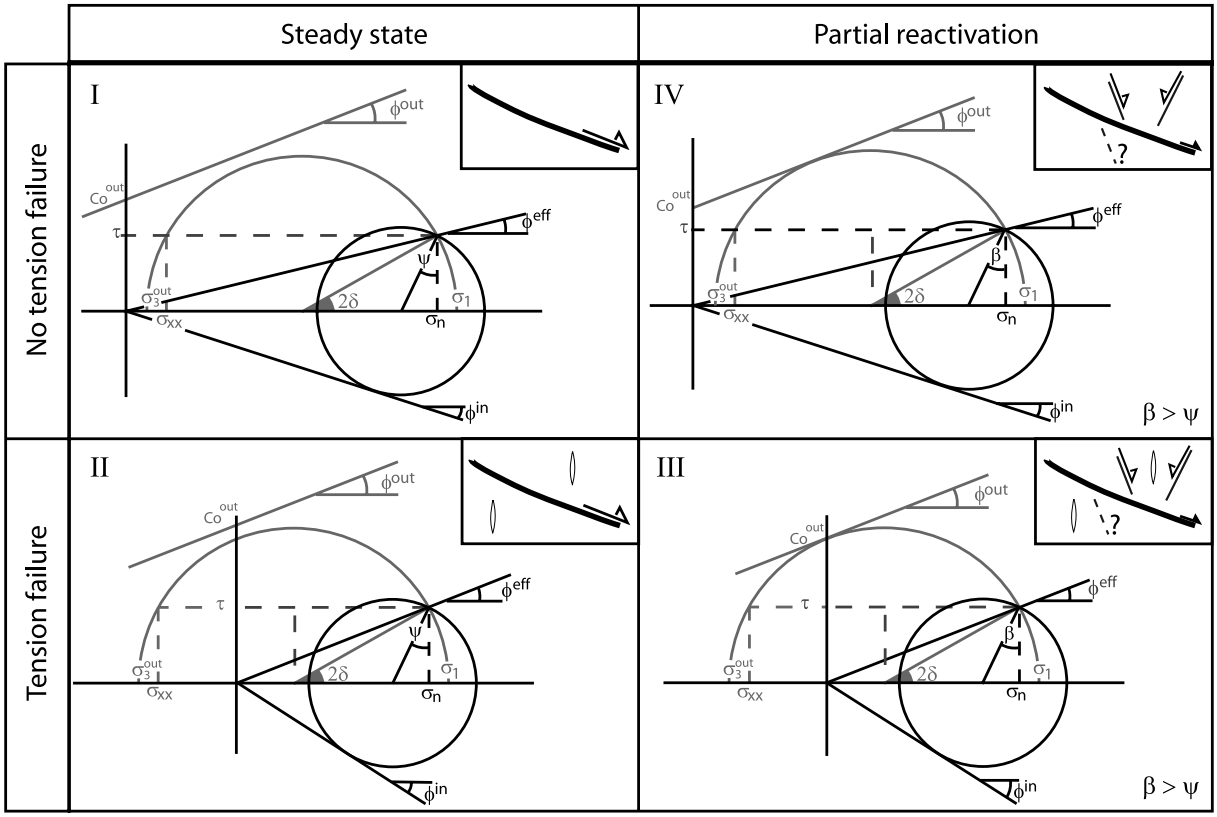

Figure 4. The four modes of reactivation including a complete or partial reactivation of the shear zone with or without tensile failure in the surrounding medium. Modes I and II suggest a steady state whereas modes III and IV suggest partial reactivation of the shear zone. Modes II and IV include the possible development of tensile failure in the surrounding medium.

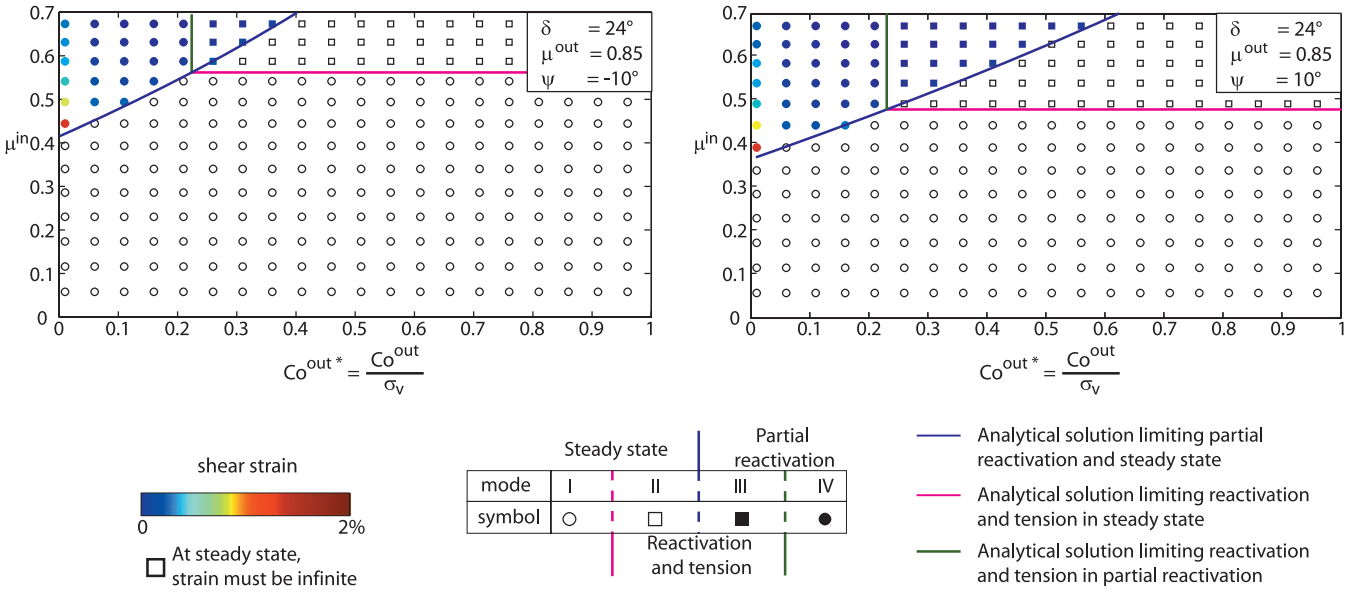

Figure 5. Plastic strain rate obtained in partial reactivation before locking as a function of the shear zone friction and the ratio between the cohesion outside the shear zone and the confining pressure Co^{out*}. Modes of reactivation are those described in Fig. 3.

reactivation model (eq. 15; Sibson 1990) as an end-member case in which rock plastic dilation ψ is equal to the friction angle ϕ. However, we proved that the angle of locking gets smaller as plastic dilation ψ decreases. For compacting shear zones ($\psi < 0$) with Byerlee friction coefficients, the locking angle may drop from 30° to 20°. Shear compaction thus allows faults dipping as shallow as 20° to be reactivated for friction consistent with laboratory observations ($\mu = 0.3$–0.5) although the classical theory would predict locking at dips of 20° for a maximum friction coefficient of 0.3. Our model also includes the incompressible model of fault reactivation such as the one proposed by Byerlee (1992) to explain the weakness of the San Andreas Fault. Interestingly, Byerlee (1992) derived this model

using slip on Riedel shears within an incompressible shear band and predicts the exact same stress rotation and effective friction drops within the shear as our model does.

3.2 Implications of the model for LANF

Repeated events of slip on a LANF alternating with formation of new high angle faults in the surrounding medium are observed in nature, the examples of the Black Mountain detachment (Death Valley, USA; Hayman *et al*. 2003) and the Cycladic detachment faults (e.g. Mehl *et al.* 2005, 2007; Jolivet *et al.* 2010) like that of Mykonos (Voreadis 1961; Skarpelis 2002; Lecomte *et al.* 2010) being representative from that mode. Those two examples differ one from each other by the development of tensile veins in the Cycladic case. However, Hayman *et al*. (2003) and Lecomte *et al.* (2010) suggest that these detachments can be active close to the surface. Those two cases fall into the partial reactivation mode described on Fig. 5. In this mode, for a dip of 15° (Mykonos detachment) and 24° (Black Mountain detachment), the model predicts friction close to 0.3 and 0.45, respectively. The friction coefficient found for the Black Mountain detachment is similar to those obtained by Hayman *et al.* (2003) using the Extensional Coulomb Wedge Model (Xiao *et al.* 1991). Considering cohesion less sedimentary rocks as Hayman *et al.* (2003) did, the ratio Co^{out*} between the cohesion of the embedded medium and the lithostatic pressure decreases to nearly 0. In that case, our model predicts a plastic strain higher than 10 per cent, which is consistent with the 14 per cent of extension observed across the fault system.

The Altotiberina fault (Apennines, Italy) is an example of an active LANF, with a dip of 15°, highlighted by microseismicity (Chiaraluce *et al.* 2007). Seismological data and seismic reflection profiles reveal the presence of steeply normal faults soling into the detachment. Chiaraluce *et al.* (2007) show that the detachment accumulated about 3 per cent of displacement at depths ranging from 3 to 15 km. In those conditions, our model predicts a friction coefficient of the fault less than 0.3. This value is consistent with average friction coefficient of 0.25–0.3 found by Collettini *et al.* (2009) for the exhumed Zuccale fault (Apennines, Italy). High fluid overpressures are related to detachments in the Apennines (Chiodini *et al.* 1999; Collettini *et al.* 2006) which helps to explain the relative low friction coefficient of those detachments (Rice 1992). However, our model does not consider fluid overpressure and its mechanical implications. This could explain the difficulties of our model to account for the coeval occurrence of high angle faults and vertical joints at high depths as described for the Zuccale fault (Collettini *et al.* 2006; Smith *et al.* 2007) or for some Cycladic detachments (Famin *et al.* 2004; Mehl *et al.* 2005).

Field observations of the above-mentioned detachments show kilometre-scale displacement. In our model, these detachments are characterized by the partial reactivation mode, which permits a significant amount of plastic strain to occur before locking. However, this plastic strain cannot explain the entire displacement on such faults and weakening processes have to be considered to allow a complete reactivation of the system and thus kilometre-scale displacement on the fault. This weakening may correspond to a decrease of the friction, of the cohesion, or of the dilation angle with increasing strain. Lavier *et al.* (1999) have shown that with a decrease of the friction or of the cohesion, it is possible to cumulate several tens of kilometers of displacement on a LANF. Since decreasing the dilation angle has a similar weakening effect on the fault zone, we believe that including a decrease with strain of the dilation angle in large strain simulations will lead to similar findings.

3.3 Predicted stress rotation versus tectonic markers in natural fault zones

As the plastic dilation angle ψ is much smaller than the friction angle ϕ in most of the natural cases, our model predicts that slip on faults will affect the orientation of the principal stress axes within the fault zone and perhaps also the slip lines within the shear zones. Elasto-plastic behaviour of faults can easily be defined by field observations (striated fault plane, brecciated gouge,. . .). However, few direct field evidence may support the compacting nature of fault zones. The stress rotation predicted by our model can nevertheless be tested through the examination of micro/meso-structures observed in natural fault zones, such as subsidiary shears like Riedel shears, among others. Fig. 6 shows the orientations of the internal shear structures (α- and β-shear bands) that should form in the shear zone as it slips in the steady state regime, for three characteristic values of dilation ($\psi = -\phi$, $\psi = 0$, and $\psi = \phi$). In the incompressible case ($\psi = 0$), we see that α- and β-shear band correspond to the R–R′ conjugate system of Riedel shear (Fig. 6) as Byerlee suggested in 1992. In the compacting shear band case ($\psi = -\phi$), the internal shear structure α is parallel to the shear zone and may correspond to the Y-band orientation that appears in mature fault zones (Tchalenko 1970). In a general case, the maximum principal stress makes an angle of $\pi/4+\psi/2$ with the shear zone and the internal shears α and β make an angle of $\pi/4-\phi/2$ with the direction of the maximum principal stress (Fig. 6). We therefore argue that accurate characterization of the orientation of subsidiary shear planes within a natural fault zone may allow to discriminate between the various possible mechanical behaviours predicted by our modelling. Especially, the occurrence of Y-bands would provide evidence for large-scale compaction of the frictional shear zone.

Stress rotation within the fault zone has also been explained by invoking a decrease of the elastic compressibility towards the fault (e.g. Faulkner *et al.* 2006). Interestingly, both the model proposed by Faulkner *et al.* (2006) and our compacting model suggest a rotation of the maximum principal stress to an angle favourable to nucleate well-oriented faults within the fault core. Whilst the two models are conceptually very different, they reach very similar predictions in term of stress orientation. In Faulkner *et al.* model (2006), the stress rotation is due to elastic strain within the shear zone prior to yielding. With that model, the fault gouge is well oriented and plastic yielding is predicted to onset in a strain-softening (i.e. unstable) regime at the scale of the fault zone.

In our model, the direction of the principal stresses rotates with plastic yielding in a hardening regime and it is only after a complete rotation that the small patches, as Riedel shears, may form in softening regime within the shear zone. In the case of a compacting fault, the patch may even be parallel to the fault zone. The apparent similarity of the behaviour of the two models relies on the fact that our elasto-plastic rigidity matrix has the same form as the anisotropic elastic rigidity matrix (e.g. Healy 2009).

3.4 Seismogenic predictions

Our model finally allows some aspects of the seismogenic behaviour of LANF zones to be captured. Any normal fault dipping between $0° < \delta < 45°$ deforms in a strain hardening regime because the effective friction of the fault increases continually with strain due

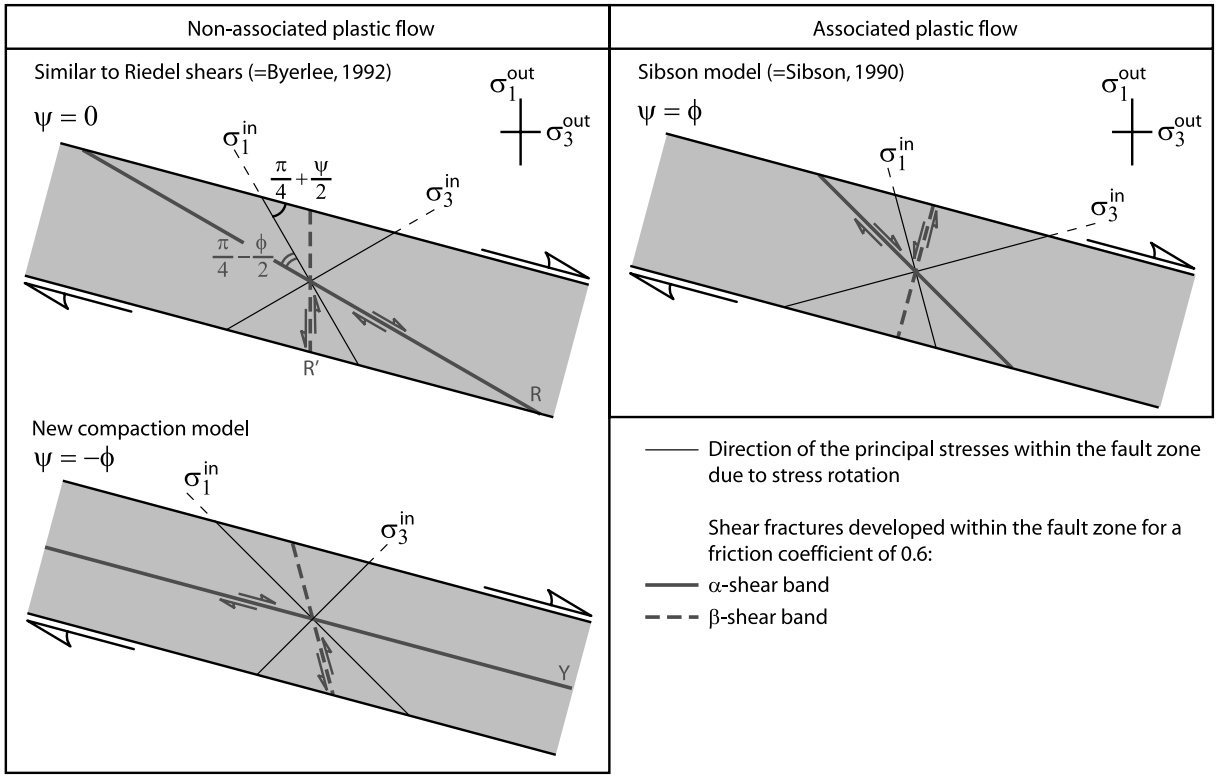

Figure 6. Predicted newly formed micro/meso-structures after the stress rotation within the fault zone for the three characteristic dilation angles ($\psi = -\phi$, $\psi = 0$ and $\psi = \phi$). For $\psi = 0$, α- and β-shear band correspond to R–R′ Riedel shears. In the compacting shear band case ($\psi = -\phi$), the α-shear band is parallel to the shear zone margin and may correspond to the Y-band orientation.

to stress rotation. In this regime, it is possible to dynamically propagate shear instabilities like earthquakes (Leroy & Ortiz 1990) but complex mechanisms, such as very high fluid overpressures (Rice 1992), are required to trigger unstable slip. However, our model would allow small earthquakes to nucleate along secondary, well-oriented faults like Riedel shears within the core of a large scale low angle shear zone behaving in a hardening regime. Slip along these Riedel faults may account for some characteristics of the microseismicity associated with active LANF zones as for instance below the Corinth Rift (Rigo *et al.* 1996); some of the multiplets observed (Pacchiani 2006) could correspond to these Riedel shears and could therefore reflect the internal slip fabric of the fault core. Our model is well in agreement with the lack of $M > 5.5$ earthquakes on LANF (Jackson & White 1989; Collettini & Sibson 2001) but allows for elasto-plastic deformation to occur aseismically on very badly oriented shear zone (with a dip less than 30°) as it is observed at the outcrop scale (e.g. Hreinsdóttir & Bennet 2009).

ACKNOWLEDGMENT

The authors thank Yves Leroy for fruitful discussions during the writing and Dave May for proof reading of the English. Thanks are due to C. Collettini, B. Holdsworth and M. Cocco who provided really useful suggestions to improve and clarify the manuscript. This paper is a contribution to the EGEO Project funded by ANR.

REFERENCES

Abers, G.A., Mutter, C.Z. & Fang, J., 1997. Shallow dips of normal faults during rapid extension: earthquakes in the Woodlark-D'Entrecasteaux rift system, Papua New Guinea, *J. geophys. Res.,* **102,** 15 301–15 317.

Anderson, E.M., 1951. *The Dynamics of Faulting and Dyke Formation with Applications to Britain,* Oliver and Boyd, Edinburgh.

Buck, W.R., 1988. Flexural rotation of normal faults, *Tectonics,* **7,** 959–973.

Byerlee, J.D., 1992. The change in orientation of subsidiary shears near faults containing high pore fluid pressure, *Tectonophysics,* **211,** 295–303.

Byerlee, J.D. & Savage, J.C., 1992. Coulomb plasticity within the fault zone, *Geophys. Res. Lett.,* **19,** 2341–2344.

Chéry, J., 2001. Core complex mechanics: From the Gulf of Corinth to the Snake Range, *Geology,* **29,** 439–442.

Chéry, J., Zoback, M.D. & Hickman, S., 2004. A mechanical model of the San Andreas fault and SAFOD Pilot Hole stress measurements, *Geophys. Res. Lett.,* **31,** 1–5.

Chiaraluce, L., Chiarabba, C., Collettini, C., Piccinini, D. & Cocco, M., 2007. Architecture and mechanics of an active low angle normal fault: Alto Tiberina Fault, northern Apennines, Italy, *J. geophys. Res.,* **112,** 1–22.

Chiodini, G., Frondini, F., Kerrick, D.M., Rogie, J., Parello, F., Peruzzi, L. & Zanzari, A.R., 1999. Quantification of deep CO2 fluxes from Central Italy. Examples of carbon balance for regional aquifers and soil diffuse degassing, *Chem. Geol.,* **159,** 205–222.

Collettini, C. & Barchi, M.R., 2002. A low angle normal fault in the Umbria region (Central Italy): a mechanical model for the related microseismicity, *Tectonophysics,* **359,** 97–115.

Collettini, C., de Paola, N. & Goulty, N.R., 2006. Switches in the minimum compressive stress direction induced by overpressure beneath a low-permeability fault zone, *Terra Nova,* **18,** 224–231.

Collettini, C., Niemeijer, A., Viti, C. & Marone, C.J., 2009. Fault zone fabric and fault weakness, *Nature,* **462,** 907–911.

Collettini, C. & Sibson, R.H., 2001. Normal faults, normal friction?, *Geology,* **29,** 927–930.

Famin, V., Philippot, P., Jolivet, L. & Agard, P., 2004. Evolution of hydrothermal regime along a crustal shear zone, Tinos island, Greece, *Tectonics,* **23,** 1–23.

Faulkner, D.R., Mitchell, T.M., Healy, D. & Heap, M.J., 2006. Slip on 'weak' faults by the rotation of regional stress in the fracture damage zone, *Nature,* **444,** 922–925.
Gerbault, M., Burov, E.B., Poliakov, A.N.D. & Daignières, M., 1999. Do faults trigger folding in the lithosphere?, *Geophys. Res. Lett.,* **26,** 271–274.
Hayman, N.W., Knott, J.R., Cowan, D.S., Nemser, E. & Sarna-Wojcicki, A., 2003. Quaternary low angle slip on detachment faults in Death Valley, California, *Geology,* **31,** 343–346.
Healy, D., 2009. Anisotropy, pore fluid pressure and low angle normal faults, *J. Struct. Geol.,* **31,** 561–574.
Hreinsdóttir, S. & Bennet, R., 2009. Active aseismic creep on the Alto Tiberina low angle normal fault, Italy, *Geology,* **37,** 638–686.
Hill, R., 1950. *The Mathematical Theory of Plasticity,* Oxford University Press, Oxford.
Jackson, J.A. & White, N.J., 1989. Normal faulting in the upper continental crust: observations from regions of active extension, *J. Struct. Geol.,* **11,** 15–36.
Jolivet, L., Lecomte, E., Huet, B., Denèle, Y., Lacombe, O., Labrousse, L., Le Pourhiet, L. & Mehl, C., 2010. The North Cycladic Detachment System, *EPSL,* **289,** 87–104.
Lavier, L., Buck, W.R. & Poliakov, A.N.B., 1999. Self-consistent rolling-hinge model for the evolution of large-offset low-angle normal faults, *Geology,* **27,** 1127–1130.
Le Pourhiet, L., Burov, E. & Moretti, I., 2004. Rifting through a stack of inhomogeneous thrusts (the dipping pie concept), *Tectonics,* **23,** 1–14.
Lecomte, E., Jolivet, L., Lacombe, O., Denèle, Y., Labrousse, L. & Le Pourhiet, L., 2010. Geometry and kinematics of Mykonos detachment (Cyclades, Greece): evidence for slip at shallow dip, *Tectonics,* **29,** doi:10.1029/2009TC002564.
Leroy, Y. & Ortiz, M., 1990. Finite element analysis of transient strain localization phenomena in frictional solids, *Int. J. Numer. Anal. Methods Geomech.,* **14,** 93–124.
Lister, G.S. & Davis, G.A., 1989. The origin of metamorphic core complexes and detachment faults formed during Tertiary continental extension in the northern Colorado River region, U.S.A., *J. Struct. Geol.,* **11,** 65–94.
McKenzie, D.P, 1969. The relation between fault plane solutions for earthquakes and the direction of the principal stress, *Bull. seism. Soc. Am.,* **59**(2), 591–601.
Mehl, C., Jolivet, L. & Lacombe, O., 2005. From ductile to brittle: evolution and localization of deformation below a crustal detachment (Tinos, Cyclades., Greece), *Tectonics,* **24,** TC4017, doi:4010.1029/2004TC001767.
Mehl, C., Jolivet, L., Lacombe, O., Labrousse, L. & Rimmele, G., 2007. Structural evolution of Andros Island (Cyclades, Greece): a key to the behaviour of a (flat) detachment within an extending continental crust, in *The Geodynamics of the Aegean and Anatolia,* Geol. Soc. London Spec. Pub., Vol. 291, pp. 41–73, eds Taymaz, T., Dilek, Y. & Ylmaz, Y., Geological Society, London.
Moore, D.E. & Rymer, M., 2007. Talc-bearing serpentinites and the creeping section of the San Andreas fault, *Nature,* **448,** 795–797.
Niemeijer, A., Elsworth, D. & Marone, C., 2009. Significant effect of grain size distribution on compaction rates in granular aggregates, *EPSL,* **284,** 386–391.
Pacchiani, F., 2006. Etudes sismologiques des failles normales actives du rift de Corinthe, *PhD thesis,* Université de Paris XI, Paris, p. 383.
Poliakov, A.N.B., Podladchikov, Y. & Talbot, C., 1993. Initiation of salt diapirs with frictional overburdens: numerical experiments, *Tectonophysics,* **228,** 199–210.
Rice, J.R., 1992. Fault stress states, pore pressure distributions, and the weakness of the San Andreas Fault, in Fault Mechanics and Transport Properties in *Rocks: A Festschrift in Honor of W.F. Brace,* pp. 475–503, eds Evans, B. & Wong, T.-F., Academic, San Diego, CA.
Rigo, A., Lyon-Caen, H., Armijo, R., Deschamp, A., Hatzfeld, D., Makropoulos, K., Papadimitriou, P. & Kassaras, I., 1996. A microseismicity study in the western part of the Gulf of Corinth (Greece): implications for large-scale normal faulting mechanisms, *Geophys. J. Int.,* **126,** 663–688.
Sibson, R.H., 1990. Rupture nucleation on unfavourably oriented faults, *Bull. seism. Soc. Am.,* **80**(6), 1580–1604.
Skarpelis, N., 2002. Geodynamics and evolution of the Miocene mineralisations in the Cycladic–Pelagonian belts, Hellenides, *Bull. geol. Soc. Greece,* **34,** 2191–2206.
Smith, S.A.F., Holdsworth, R.E., Collettini, C. & Imber, J., 2007. Using footwall structures to constrain the evolution of low angle normal faults, *J. geol. Soc., London,* **164,** 1187–1191.
Tchalenko, J.S., 1970. Similarities between Shear Zones of Different Magnitudes, *Bull. geol. Soc. Am.,* **81,** 1625–1640.
Vermeer, P., 1990. The orientation of shear bands, *Geotechnique,* **40**(2), 223–234.
Vermeer, P. & de Borst, R., 1984. Non-associated plasticity for soils, concrete and rock, *Heron,* **29,** 1–64.
Voreadis, G.D., 1961. Die Geologie und die Barytlagerstätten der Inseln Mykonos and Dragonissi, *Annales géologiques des Pays Helléniques,* **12,** 263–300.
Wernicke, B., 1981. Low angle normal faults in the Basin and Range province: Nappe tectonics in an extending orogen, *Nature,* **291,** 645–648.
Wernicke, B., 1992. Cenozoic extensional tectonics of the U.S. cordillera, in *The Cordilleran Orogen: Conterminous U.S,* pp. 553–581, eds Burchfiel, B.C., Lipman, P.W. & Zoback, M.L., Geological Society of America, Boulder, CO.
Xiao, H.B., Dahlen, F.A. & Suppe, J., 1991. Mechanics of extensional wedges, *J. geophys. Res.,* **96,** 10 301–10 318.

APPENDIX A: ELASTO-PLASTIC RHEOLOGY

The elasto-plastic strain rate is decomposed into an elastic $\dot{\varepsilon}^e$ and a plastic $\dot{\varepsilon}^p$ components assuming their summation:

$$\dot{\boldsymbol{\varepsilon}} = \dot{\boldsymbol{\varepsilon}}^e + \dot{\boldsymbol{\varepsilon}}^p. \tag{A1}$$

Applying Hooke's law, the elastic strain rate can be related to the stress rate:

$$\dot{\boldsymbol{\varepsilon}}^e = \boldsymbol{D}^{-1}\dot{\boldsymbol{\sigma}}. \tag{A2}$$

The rigidity matrix D is expressed in terms of shear modulus G and the Poisson's ratio ν:

$$\boldsymbol{D} = 2G \begin{bmatrix} \frac{(1-\upsilon)}{1-2\upsilon} & \frac{\upsilon}{1-2\upsilon} & 0 \\ \frac{\upsilon}{1-2\upsilon} & \frac{(1-\upsilon)}{1-2\upsilon} & 0 \\ 0 & 0 & \frac{1}{2} \end{bmatrix}. \tag{A3}$$

The plastic potential $\mathcal{Q}$ (eq. A4) differs from the yield criterion $\mathcal{F}$ in that the dependence upon pressure is expressed in terms of plastic dilation ψ rather than friction ϕ:

$$\mathcal{Q} = \tau^* - \sigma^* \sin\psi. \tag{A4}$$

The plastic flow is expressed as the derative of the plastic potential function versus stress multiplied by a plastic scalar multiplier $\dot{\lambda}$:

$$\dot{\boldsymbol{\varepsilon}}^p = \dot{\lambda}\frac{\partial \mathcal{Q}}{\partial \boldsymbol{\sigma}}. \tag{A5}$$

It results that the plastic flow is not normal to the yield envelope unless $\psi = \phi$, therefore the plastic flow considered here is said non-associated. Assuming that the fault continues to yield, that is, $\dot{\mathcal{F}} = 0$, it is possible to write $\dot{\lambda}$ as a function of strain rate to build the elasto-plastic rigidity matrix according to Hill (1950):

$$\dot{\boldsymbol{\sigma}} = \left[\boldsymbol{D} - \frac{1}{d}\boldsymbol{D}\frac{\partial \mathcal{Q}}{\partial \boldsymbol{\sigma}}\frac{\partial \mathcal{F}}{\partial \boldsymbol{\sigma}}\boldsymbol{D}\right]\dot{\boldsymbol{\varepsilon}}, \tag{A6}$$

where d is a scalar plastic hardening modulus defined as $d = \frac{\partial \mathcal{F}}{\partial \boldsymbol{\sigma}}\boldsymbol{D}\frac{\partial \mathcal{Q}}{\partial \boldsymbol{\sigma}}$.

SUPPORTING INFORMATION

Additional Supporting Information may be found in the online version of this article:

Figure A1. Stress evolution using Mohr circles of the extensional reactivation of a well-oriented normal fault. The black point corresponds to the fault plane. Stresses are normalized to σ_v.
Figure A2. Stress evolution using Mohr circles of the extensional reactivation of a badly-oriented normal fault. The black point corresponds to the fault plane. Stresses are normalized to σ_v.

Figure A3. Stress evolution using Mohr circles of the partial extensional reactivation of a badly-oriented normal fault. The black point corresponds to the fault plane. Stresses are normalized to σ_v. The locking of the fault occurs when stresses outside the shear zone (blue circle) reach the yield criterion.

Please note: Wiley-Blackwell are not responsible for the content or functionality of any supporting materials supplied by the authors. Any queries (other than missing material) should be directed to the corresponding author for the article.